Spectral variability and reverberation time delays in the *Suzaku* X-ray spectrum of NGC 4051

L. Miller,[1]★ T. J. Turner,[2,3] J. N. Reeves,[4] A. Lobban,[4] S. B. Kraemer[3,5] and D. M. Crenshaw[6]

[1]*Department of Physics, Oxford University, Denys Wilkinson Building, Keble Road, Oxford OX1 3RH*
[2]*Department of Physics, University of Maryland Baltimore County, Baltimore, MD 21250, USA*
[3]*Astrophysics Science Division, NASA/GSFC, Greenbelt, MD 20771, USA*
[4]*Astrophysics Group, School of Physical and Geographical Sciences, Keele University, Keele, Staffordshire ST5 8EH*
[5]*Institute for Astrophysics and Computational Sciences, Department of Physics, The Catholic University of America, Washington, DC 20064, USA*
[6]*Department of Physics and Astronomy, Georgia State University, Astronomy Offices, One Park Place South SE, Suite 700, Atlanta, GA 30303, USA*

ABSTRACT

Long-exposure *Suzaku* X-ray observations of the nearby active galaxy NGC 4051 from 2005 and 2008 are analysed, in an attempt to reach a self-consistent understanding of both the spectral variability on long time-scales and the broad-band variability at high time resolution. The techniques of principal components analysis and a maximum likelihood method of power spectrum analysis are used. In common with other type I active galactic nuclei (AGN), the spectral variability is dominated by a varying-normalization power-law component together with a quasi-steady, hard-spectrum offset component that contains Fe K atomic features. NGC 4051 displays a strong excess over a power law at energies of above 20 keV, some fraction of which also appears to vary with the power-law continuum. The fast time-scale power spectrum has a shape generally consistent with previous determinations, with the previously known dependence on broad-band photon energy, but in the new data significant differences are found between the low and high flux states of the source, demonstrating that the power spectrum is non-stationary. Frequency-dependent time lags between the hard and soft bands of up to 970 ± 225 s are measured. The existence of the observed time lags excludes the possibility that the hard spectral component originates as reflection from the inner accretion disc. We instead show that the time lags and their frequency and energy dependence may be explained simply by the effects of reverberation in the hard band, caused by reflection from a thick shell of material with maximum lags of about 10 000 s. If the reflecting material surrounds the AGN, it extends to a distance of about 1.5×10^{14} cm, 600 gravitational radii, from the illuminating source and the global covering factor is $C_\mathrm{g} \gtrsim 0.44$, confirming previous suggestions that type I AGN have high covering factors of absorbing and reflecting material. Given the spectral and timing similarities with other type I AGN, we infer that this source structure is common in the type I population.

Key words: accretion, accretion discs – galaxies: active – X-rays: galaxies – X-rays: individual: NGC 4051.

1 INTRODUCTION

Given the impossibility of imaging the innermost regions of active galactic nuclei (AGN) at X-ray energies, the principal tools for studying accretion in this waveband have been either modelling of X-ray spectra or studying the rapid X-ray variability of nearby, bright AGN. Owing to signal-to-noise ratio limitations, spectral analysis has tended to concentrate on fitting simple composite models to mean spectra (e.g. Miniutti et al. 2007). For the same reason, timing analyses have studied the variability on short time-scales but in broad bandpasses of photon energy (e.g. McHardy et al. 2004). To date, conclusions from these studies have not been combined in a self-consistent way. However, there is substantially more information available in the spectral variability than is contained in the mean spectrum alone, and now that some long-exposure observations have been made, those data may be time-sliced and the spectral variability used as a powerful constraint on the models (e.g. Miller et al. 2007; Miller, Turner & Reeves 2008). Long-exposure observations have

★E-mail: L.Miller@physics.ox.ac.uk

also revealed interesting variability signatures on short time-scales (see below). In this paper, we aim to carry out both spectral variability and timing analysis on long-duration *Suzaku* observations of the nearby AGN NGC 4051 and to reach a consistent understanding of the source behaviour.

There are two phenomena of particular interest in each of the 'spectral variability' and the 'timing' domains. The first is that it is now well established that type I AGN frequently show a broad 'red wing' of emission extending below the 6.4 keV Fe Kα emission line that appears as an excess above a model power-law continuum (e.g. Tanaka et al. 1995), and this has been widely interpreted as being Fe Kα emission from within a few Schwarzschild radii of the black hole. Model fits to mean spectra infer a redshift so large that the emission would need to come from within the innermost stable circular orbit of a Schwarzschild black hole, leading to claims of the detection of black hole spin in these AGN (e.g. Wilms et al. 2001). However, a particular problem is that any Fe Kα emission should vary in phase with the illuminating continuum, whereas the red wing appears to be largely invariant while the illuminating source appears to exhibit large time variations (e.g. Iwasawa et al. 1996; Vaughan & Fabian 2004). The problem is now known to extend to high energies: above 20 keV many AGN have an excess of continuum compared with extrapolation of a 2–10 keV power-law model, and this has been supposed to be continuum reflection (Compton scattering modified by the photoelectric opacity of the gas) from the same material that produces the red wing. Indeed, this 'hard excess' is likewise known to exhibit little variability compared with the 2–10 keV band, pointing to a common origin with the red wing (Miniutti et al. 2007). However, its flux is so large that it cannot readily be ascribed to reflection unless the illuminating source is significantly obscured along our line of sight (e.g. Terashima et al. 2009).

To overcome these problems, Fabian & Vaughan (2003), Miniutti et al. (2003) and Miniutti & Fabian (2004) have proposed a 'light-bending' model in which the effect of light following geodesics near the black hole means that a reflection component from the inner accretion disc may be made relatively invariant, if it is illuminated by a source whose position changes with respect to the disc. The model requires both that the illuminating source be compact, comparable in size to the event horizon, and move towards and away from the disc. As it moves, the flux received by a distant observer varies as light is removed from the line of sight. In this model, it is the change in position of the primary source that dominates the observed variability, rather than intrinsic fluctuations. The light bending could also explain the high apparent reflectivity in the hard band. However, Miller et al. (2008) and Miller, Turner & Reeves (2009) have shown that the red wing and the hard excess in MCG−6-30-15 may instead be explained by the spectrum expected from clumpy, 'partial-covering' absorbers and that a model in which the absorber covering fraction varies provides a good description of the observed spectral variability, as well as of the mean spectrum of this AGN. Both Compton-scattering reflection and absorption shape this hard spectral component, but the relative importance of scattering/reflection and absorbed transmission is not yet established (Miller et al. 2009).

The second important phenomenon occurs in the timing domain. There are now a significant number of AGN where time lags in the range of tens to thousands of seconds between different spectral bands are seen, in the sense that hard-band photons lag soft band (Papadakis, Nandra & Kazanas 2001; Vaughan, Fabian & Nandra 2003; McHardy et al. 2004; Markowitz 2005; Arévalo et al. 2006; Markowitz et al. 2007; Arévalo, McHardy & Summons 2008). Im-

portantly, the lags are dependent on the frequency of the source variation in the sense that if a source's variations are decomposed into Fourier modes, the lag between hard and soft energy bands increases with the period of those modes and also increases with the separation in the energy of the bands. The lags and their frequency dependence have been explained by a model comprising perturbations propagating inwards on an accretion disc where harder X-ray emission is emitted from smaller radii (Arévalo & Uttley 2006). Although the initial observations were consistent with a linear relationship with the Fourier period, recently, more complex behaviour has been seen, leading to a hypothesis that fluctuations arise in multiple components (McHardy et al. 2007). However, this explanation of rapid fluctuations propagating through the accretion disc is not consistent with the light-bending model, which has the primary variations caused by motion of the hypothesized compact source above the accretion disc. It is our aim in this paper to reconcile the phenomena of spectral variability and time lags in a detailed study of NGC 4051.

NGC 4051 is a well-studied, nearby narrow-line type I AGN with redshift $z = 0.0023$. If the redshift were purely due to cosmological Hubble flow, its distance would be 9.3 Mpc for Hubble's constant $H_0 = 74 \, \text{km s}^{-1} \, \text{Mpc}^{-1}$, but for such a nearby galaxy the Tully–Fisher distance is probably more reliable, placing it at 15.2 Mpc (Russell 2004). It has a black hole mass determined from optical reverberation mapping of $M_{BH} = 1.7^{+0.55}_{-0.52} \times 10^6 \, M_{\odot}$ (Denney et al. 2009). It has long been known to be highly variable on short time-scales at X-ray energies, with spectral variability that is correlated with flux (Lawrence et al. 1985, 1987; Matsuoka et al. 1990; Kunieda et al. 1992; McHardy et al. 1995; Lamer et al. 2003). The timing properties of X-ray observations with the *Rossi X-ray Timing Explorer* (*RXTE*) and *XMM–Newton* have been studied in detail by McHardy et al. (2004). The X-ray spectrum has previously been studied by Guainazzi et al. (1996, 1998) and Pounds et al. (2004), among others. Of particular interest is a 2005 *Suzaku* observation obtained when the source was in a low state that reveals a strong excess of emission above a power law at energies $E \gtrsim 20 \, \text{keV}$ (Terashima et al. 2009). Overall, the consensus from recent analyses is that NGC 4051 has low states where the primary power-law source has largely disappeared and where the remaining emission appears to be dominated by reflected emission (Guainazzi et al. 1998; Pounds et al. 2004; Terashima et al. 2009). Terashima et al. (2009) found that partially covered reflection was required to fit the hard excess rather than supposing this to be inner disc gravitationally redshifted reflection. The high variability on short time-scales means that this AGN provides a powerful testbed for using spectral variability and power spectrum analysis methods to untangle the source emission components.

We now consider both the 2005 *Suzaku* observation and two new *Suzaku* observations obtained in 2008 and analyse both the time-dependent spectrum and the high time resolution behaviour.

2 OBSERVATIONS AND DATA REDUCTION

The *Suzaku* data analysed here were reduced as described by Turner et al. (2009b) and Lobban et al. (in preparation). The *Suzaku* X-ray Imaging Spectrometer (XIS; Koyama et al. 2007) comprises four X-ray telescopes (Mitsuda et al. 2007), each with a CCD detector. XIS CCDs 0, 2, 3 are configured to be front-illuminated and yield useful data over ∼0.6–10.0 keV with energy resolution full width at half-maximum (FWHM) of ∼150 eV at 6 keV. XIS 1 is a back-illuminated CCD and has an enhanced soft-band response down to 0.2 keV but a lower area at 6 keV than the front-illuminated CCDs,

Table 1. Summary of the three *Suzaku* observations, giving the ID number, dates, the detectors used in the analysis, total duration, xis on-source time, the mean xis count rate in the 0.3–10 keV range and the mean flux in the 2–10 keV range. The 2005 count rate has been scaled to the value for two detectors, for consistency with the 2008 observations.

ID	Dates	Detectors	Duration (s)	On-time (s)	Mean count rate (s^{-1})	Mean 2–10 keV flux (10^{-11} erg s^{-1} cm^{-2})
700004010	2005 Nov 10–13	xis 0, 2, 3, pin	222 592	119 618	0.93	0.87
703023010	2008 Nov 6–12	xis 0, 3, pin	494 834	274 531	4.19	2.41
703023020	2008 Nov 23–25	xis 0, 3, pin	161 695	78 394	2.87	1.79

as well as a higher background level at high energies. xis 1 was not used in our analysis. Use of xis 2 was discontinued after a charge leak was discovered in 2006 November, so we used data from xis 0, 2 and 3 in 2005 and data from xis 0 and 3 in 2008.

Our analysis used three observations from 2005 November 10–13, 2008 November 6–12 and 2008 November 23–25. The data were reduced using v6.4.1 of HEAsoft and screened to exclude periods (i) during and within 500 s of the South Atlantic Anomaly, (ii) with an Earth elevation angle of less than 10° and (iii) with a cut-off rigidity of >6 GeV. The source was observed at the nominal pointing for the xis. The front-illuminated CCDs were in 3 × 3 and 5 × 5 edit modes, with a normal clocking mode. For the xis, we selected events with grades 0, 2, 3, 4 and 6 and removed hot and flickering pixels using the SISCLEAN script. The spaced-row charge injection was used. The xis products were extracted from circular regions of 2.9 arcmin radius with background spectra from a region of the same size, offset from the source (avoiding the calibration sources at the edges of the chips). The response and ancillary response files were created using XISRMFGEN v2007 MAY and XISSIMARFGEN v2008 MAR.

Suzaku also has a non-imaging, collimated hard X-ray detector (HXD; Takahashi et al. 2007) whose pin instrument provides useful data over 15–70 keV for bright AGN. NGC 4051 is too faint to be detected by the HXD GSO instrument, but was detected in the pin. For the analysis, we used the model 'D' background (Fukazawa et al. 2009). As the pin background rate is strongly variable around the orbit, we first selected source data to discard events within 500 s of a South Atlantic Anomaly passage; we also rejected events with day/night elevation angles of >5°. The time filter resulting from the screening was then applied to the background events model file to give pin model background data for the same time intervals covered by the on-source data. As the background events file was generated using 10 times the actual background count rate, an adjustment to the background spectrum was applied to account for this factor. HXDDTCOR v2007 MAY was run to apply the deadtime correction to the source spectrum. As the pin deadtime correction varies, for the time-dependent analysis below, the correction was calculated at 128 s time resolution and the mean correction in each analysed time interval was applied to the source counts.

The observations are summarized in Table 1, which also gives the xis count rates and the flux integrated over 2–10 keV. The 2005 observation caught NGC 4051 in a historical low state, while in 2008 the source flux was more typical and close to the value in the 2001 *XMM–Newton* data analysed by McHardy et al. (2004).

3 SPECTRAL VARIABILITY ON TIME-SCALES LONGER THAN 20 KS

3.1 Principal components analysis

Our first step to understanding the variations in NGC 4051 is to carry out a principal components analysis (PCA) of the spectral variations.

This is a method of decomposing the variations into orthogonal components, eigenvectors. By ordering the eigenvectors according to their eigenvalues, we can extract the principal modes of variation. It is particularly well suited to variations that are additive in nature (such as variations in the partial-covering fraction by a clumpy absorber). We use the method described in detail by Miller et al. (2007), in which spectral bins are created of width equal to half the energy-dependent instrument resolution. Spectra are averaged over and sampled at time intervals that are sufficiently long that variations between time samplings are dominated by intrinsic variations rather than shot noise. The method uses singular value decomposition to cope with the problem that there are more spectral points than there are available time bins; in this case, the leading eigenvectors are still defined and may be extracted.

In interpreting the results, there should be no expectation that the orthogonal eigenspectra produced correspond uniquely to any physical component in the AGN. However, what has been found in previous analyses of other AGN (Miller et al. 2007, 2008) is that only a small number of variable components are required to describe the spectral variability, which is indicative that additive processes are at work. In those previous analyses we concentrated on eigenvector one, which describes the primary source variation, and subsumed the rest of the source spectrum into an 'offset' component which is essentially steady in time (see Miller et al. 2007; Turner et al. 2007 for more detailed discussion). The offset component is not uniquely defined because we are free to add or subtract arbitrary amounts of eigenvector one without changing the decomposition. However, we may define a minimum offset component by requiring that no spectral bin have negative flux and a maximum offset component by requiring that no spectral bin be higher than the lowest observed value.

3.2 Spectral variability

Fig. 1 shows the mean spectra from 2005 and 2008 November 6–12, plotted as unfolded spectrum against a power law with photon index $\Gamma = 2$. In the figure, cosmic X-ray background has been subtracted from the pin data by using XSPEC v 11.3.2ag to generate a spectrum from a cosmic X-ray background model (Gruber et al. 1999) normalized to the 34 × 34 $arcmin^2$ pin field of view, which was then combined with the pin instrument background file. No correction for the calibration difference between the xis and pin instruments has been applied in Fig. 1; this has the effect of making the pin data too high by 16 per cent relative to the xis data. The basic spectral variability mode of the source is clearly seen, with the hard, low-state and higher softer spectrum at the two epochs. There is a significant hard excess above 20 keV, which has varied between the epochs. In 2008, there is also a 'red wing' as an excess above a power-law continuum below the 6.4 keV Fe Kα line; in the 2005 data, this can be seen to have developed into a rather different continuum shape. Previous analyses have assumed the red wing
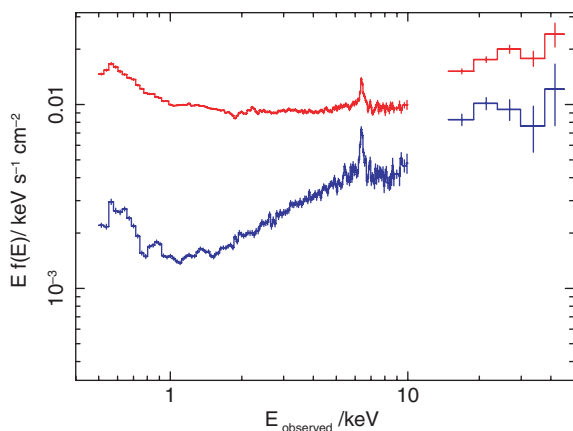
Figure 1. Combined XIS and PIN spectra of NGC 4051 from 2005 (lower curve) and 2008 November 6–12 (upper curve), plotted as $E f(E)$, unfolded against a power law with photon index $\Gamma = 2$. XIS data have been binned at the instrumental HWHM and PIN data at intervals $\Delta \log_{10} E = 0.1$. Photon shot noise errors are shown. No cross-calibration correction between XIS and PIN instruments has been applied in this figure.

to be relativistically broadened Fe Kα emission (e.g. Lamer et al. 2003), but this interpretation is not obviously supported by the PCA.

The PCA of the observations in the energy range of 0.4–50 keV is shown in Fig. 2. The time sampling was 20 ks; although this source is highly variable on shorter time-scales, it is important to avoid the regime where counts in each spectral bin are dominated by shot noise. The full 2005–2008 data set was used, incorporating both XIS and PIN data. XIS data were binned at the spectral resolution half-width at half-maximum. To achieve an adequate signal-to-noise ratio in the PIN data, coarser spectral binning was used ($\Delta \log_{10} E = 0.1$). The minimum and maximum limits on the offset component are shown, together with the contribution of the CXB that has been subtracted from the PIN offset component. The PIN data have been reduced by the 16 per cent cross-calibration factor between the XIS and PIN instruments. Uncertainties on each spectral point were obtained by a Monte Carlo method as described by Miller et al. (2007). Eigenvector one accounts for 81 per cent of the variance in this energy band. Eigenvector two accounts for a further 11 per cent of the variance, and although noisy this component appears dominated by a residual anticorrelation between the PIN and XIS data, which when considered with the eigenvector one spectrum implies

that there is a minor element of uncorrelated variation between the XIS and PIN bands. In this paper, we shall concentrate on the gross spectral variability characterized by eigenvector one and the offset component.

The PCA shows the same generic features as the other type I AGN that it has been applied to (e.g. Mrk 766, Miller et al. 2007; MCG−6-30-15, Miller et al. 2008). The hard offset component dominates the PIN band and contains atomic signatures, particularly of the Fe K edge and Fe Kα emission line, indicative of the importance of atomic processes in shaping this component. Eigenvector one is essentially a power law, but with some 'warm absorber' signatures imprinted on it in the soft band and, unusually, evidence of both an excess variable component above 20 keV and weak evidence for broadened Fe Kα emission, with an equivalent width of about 66^{+43}_{-37} eV. The width of the broad component is not well constrained, but there is no evidence for any excess variable component below 6 keV, and in common with other AGN, the 'red wing' component is described by the constant offset spectrum: the red wing feature in the 2008 data is implied by the PCA to be simply a sum of the very hard-spectrum offset component and the power-law-like eigenvector one.

The interpretation of eigenvector one is fairly straightforward, as it implies that the primary continuum has a power-law form of an invariant index, whose amplitude varies. The amplitude variations could either be intrinsic to the source producing the power law or could arise from changes in the covering fraction of an external absorber. The variable hard excess could either be flux transmitted through a partially covering, high column density absorber, such as found in PDS 456 (Reeves et al. 2009) and 1H 0419–577 (Turner et al. 2009a), or could arise as reflection from optically thick, or nearly so, material. If there are high column density partial-covering absorbers, we expect to see both transmitted flux at high energy and Compton-scattered flux (see Miller et al. 2009).

The offset component, which essentially describes the source in its lowest observed flux state, may be explained either as being dominated by reflection from optically thick material or as being the residual signal that arises from partial-covering variations. These possibilities are discussed more by Miller et al. (2007) and Turner et al. (2007), where the point is made that it is fundamentally not possible to distinguish between these possibilities by continuum fitting alone. Although spectral models have previously tended to be characterized as being dominated by either one or other of absorption or reflection, it now seems likely that both physical processes
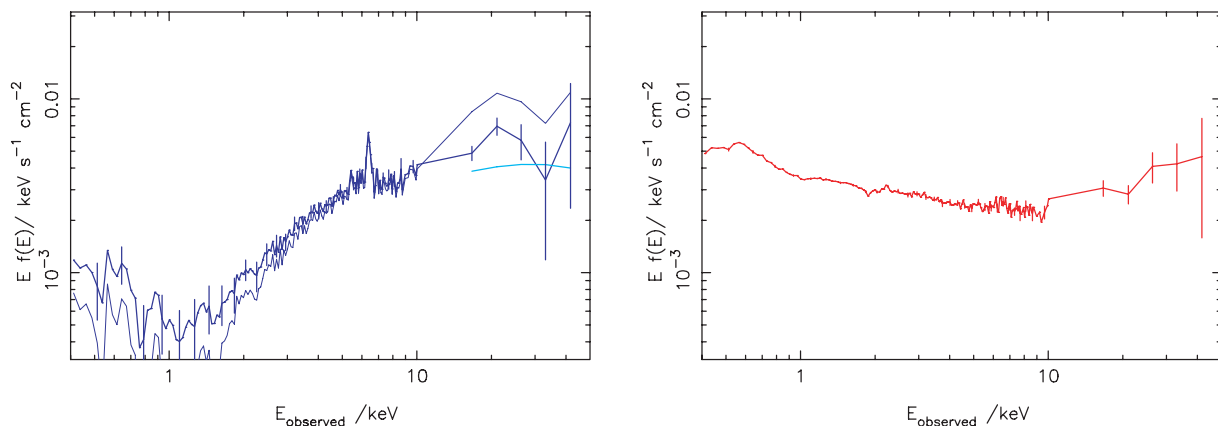
Figure 2. PCA of the combined 2005–2008 data set for NGC 4051. Left: the offset component, showing the possible range of this component (upper and lower curves) and the component of CXB that has been subtracted (solid curve). For clarity, errors are shown only every fifth point on one of the offset spectra. Right: eigenvector one.

make significant contributions; absorbing zones of high column density also contribute a significant flux of Compton-scattered light (Miller et al. 2009). We return to discussion of the interpretation of the spectral variability in Section 5, after consideration of the variability on shorter time-scales.

Finally, the Fe Kα emission is particularly interesting.[1] The narrow 6.4 keV line, produced by Fe I–XVII, appears only on the offset component, and hence must have had an invariant flux in the 2005 and 2008 epochs. The implication is that the gas responsible for the line experienced the same ionizing continuum in 2005 as in 2008, despite the observed 7–10 keV flux being a factor of 2.5 higher in 2008 than in 2005. We discuss later the interpretation that the dip into the 2005 low state was caused by obscuration along our line of sight.

3.3 Summary of key spectral variability results

We summarize the key points from the above, to aid the later discussion.

(i) NGC 4051 shows the same general form of spectral variability as other type I AGN, with a soft varying power law and a less variable hard-spectrum component that creates a red wing below 6.4 keV and PIN-band excess above the power law in the mean spectrum. The 2005 low state is dominated by this hard component. The new analysis confirms the conclusions of Pounds et al. (2004) and Terashima et al. (2009).

(ii) The 6.4 keV Fe Kα narrow emission line was unchanged between 2005 and 2008 despite a significant change in the continuum flux, as also discussed by Pounds et al. (2004).

(iii) There is also a component of variable hard excess at $E \gtrsim 20$ keV that varies with the power-law continuum on 20 ks time-scales, with evidence for an associated Fe Kα line component that is moderately broadened (i.e. not relativistically broadened), by either Doppler- or Compton-scattering effects.

4 POWER SPECTRUM AND TIME DELAY MEASUREMENT

4.1 Maximum-likelihood estimation of the power spectrum and time delays

We now wish to complement the spectral variability analysis with analysis of the spectral variations in broader energy bands on shorter time-scales. In the case of *Suzaku* observations, it is not possible to use periodogram-type methods (e.g. Papadakis & Lawrence 1993) because of the substantial gaps in the data caused by the filtering of events and the short orbital time-scale. Table 1 shows that the fraction of usable data is in the range of 0.48–0.55. Furthermore, the orbital period imposes regular gaps of a period of 5753 s on the data. Instead we use a maximum likelihood method, based on that of Bond, Jaffe & Knox (1998), which is described more fully in the context of X-ray time series analysis by Miller (in preparation). The reader is referred to that paper for a full description of the method, but briefly, we start by defining the power spectral density (PSD), $P(\nu)$, as the Fourier transform of the autocorrelation function, $\mathcal{A}(\tau)$:

$$\mathcal{A}(\tau) = \int_{-\nu_{\max}}^{\nu_{\max}} d\nu\, P(\nu) \cos(2\pi\nu\tau) \operatorname{sinc}^2\left(\frac{\pi\nu}{2\nu_N}\right), \quad (1)$$

where ν_N is the sampling Nyquist frequency (we assume uniform sampling in time) and the sinc^2 term arises from the effect of binning the counts in bins of duration equal to the time sampling (see also Efstathiou & Moody 2001). We do not construct a periodogram, but instead use an iterative maximum likelihood method to find the best-fitting coefficients for a model PSD given the measured time series. We adopt a Gaussian likelihood function, $\mathcal{L}$, which thus takes the form

$$\mathcal{L} = \frac{1}{(2\pi)^{N/2} |C|^{1/2}} \exp\left[-\frac{1}{2}\Delta^T C^{-1}\Delta\right], \quad (2)$$

for a time series containing N data samples, where C is an $N \times N$ model covariance matrix and Δ is the time series of fractional fluctuations of length N. To find the best-fitting PSD, we compute the expected covariance matrix for an initial set of model parameter values using equation (1) and iterate. Because we can calculate the derivatives of the likelihood function with respect to the model, from equation (1), we can use a Newton-type method as described by Bond et al. (1998), and the iterations typically converge within five iterations to a stable solution irrespective of the number of model parameters.

The PSD model we adopt follows Bond et al. (1998) in defining a set of 'bandpowers', which we choose to be stepwise in νP_ν:

$$\mathcal{A}(\tau) = 2\sum_i \int_{\nu_{1,i}}^{\nu_{2,i}} \frac{d\nu}{\nu}(\nu_i P_i) \cos(2\pi\nu\tau) \operatorname{sinc}^2\left(\frac{\pi\nu}{2\nu_N}\right), \quad (3)$$

where each bandpower has PSD amplitude P_i in the frequency range $\nu_{1,i}-\nu_{2,i}$. Within each band the PSD is constant in $\nu P(\nu)$, which helps reduce sharp steps in the PSD at bandpower edges compared with defining bandpowers uniform in $P(\nu)$. As part of the likelihood maximization procedure, we calculate the Fisher matrix for the PSD coefficients, allowing us to have estimates of the errors and their covariance. These errors include the sampling uncertainty that arises because we only observe a finite time series. The likelihood estimation is in the time domain, so the errors on the PSD coefficients are well understood even in the presence of a complex sampling window function. The method is immune to gaps in the data, periodic or otherwise (if the time sampling is such that one particular Fourier mode is badly sampled, this is simply reflected in the corresponding uncertainty). Multiple data sets spanning arbitrarily long time baselines may be trivially combined, so we are able to analyse the three *Suzaku* observations as either individual or combined time series.

The likelihood function that is maximized includes terms in the autocorrelation function for both modes intrinsic to the source, described by $P(\nu)$, and Poisson shot noise. Thus, the likelihood method automatically corrects for Poisson noise in the data and is accurate even in the low count rate regime. Because the shot noise is put into the likelihood model, the uncertainties on the PSD that we measure include the statistical uncertainty arising from shot noise. Although correction for high-frequency aliasing may also be included in this method (Miller, in preparation), as both the high-frequency part of the PSD has a steep spectrum, $P_\nu \propto \nu^{-\alpha}$ where $\alpha \simeq 2.1$ (McHardy et al. 2004), and also aliased high-frequency modes are suppressed by the sinc^2 term, the effects of aliasing are minimal and we make no aliasing correction.

The likelihood method may be extended to simultaneously measure the PSDs of two time series, and their cross-spectrum frequency-dependent coherence and time delays (Miller, in preparation), and we show results from this analysis also. By incorporating time delays as additional parameters in the likelihood model we can straightforwardly compute best-fitting values and errors.

---

[1] Turner et al. (2009b) also discuss the companion line visible at 5.44 keV in the offset spectrum.

4.2 Red noise leak and the PSD bandpower widths

A well-known problem with any power-spectrum estimation method applied to finite time series is that modes on time-scales longer than the window function are not correctly measured. In effect, long-time-scale variations are interpreted instead as modes with periods on the scale of the window function, a phenomenon known as 'red noise leak'. If the variations do not have much power on long time-scales this may not be important, but as NGC 4051 has a low-frequency PSD $P(\nu) \propto \nu^{-\alpha}$ where $\alpha \simeq 1$ at least down to $\nu \lesssim 10^{-8}$ Hz (McHardy et al. 2004), red noise leak cannot be ignored. Miller (in preparation) has tested the effect of red noise leak using data simulated with the McHardy et al. (2004) PSD of NGC 4051 and sampled with the window function provided by the 2008 *Suzaku* observations. As expected, it is found that the lowest frequency periods are measurably affected by red noise leak. In principle in our PSD estimator we can include low-frequency modes by extrapolating the lowest bandpower down in frequency; however even this is not a good solution as in the data we are not averaging over a large number of low-frequency modes, and furthermore the analysis becomes dependent on the model assumed for the extrapolation.

A related issue is that modes close in frequency are statistically correlated because of the finite window function. We must therefore choose frequency widths for our bandpower estimates that are broader than the window function to avoid unpleasant correlations and degeneracies between neighbouring bandpowers. At the lowest frequency bandpowers, the effect of red noise leak also introduces correlations and anticorrelations between neighbouring modes. The best solution is to choose bandpowers that are fairly broad. In the following analysis, we choose bandpowers that are logarithmically spaced, with $\Delta \log_{10} \nu = 0.4$ or 0.5; at high frequencies, this is adequate to ensure that they are independent. At low frequencies, we bin together those bandpowers to make a single bandpower whose width is at least as large as the half-power full-width (HPFW) of the window function. We measure the HPFW by direct Fourier transform of the window function, and find the frequency lower than which half the summed power is found. The lowest frequency bandpower in our analysis thus tends to be extremely broad in $\log \nu$.

Because of red noise leak, the PSD in this lowest bandpower should always be treated with caution in the subsequent analysis. One particular concern which arises is in the measurement of time lags between energy bands. A long-period mode which has some small time shift between two energy bands will, in the low-frequency limit, simply appear as having a shift in the mean value between the bands within the observed time window. The shift in the mean will be removed because we use the observed mean value to convert the measured time series into fractional fluctuations Δ, and hence the time lag will disappear. We return to this concern in Sections 4.3.4 and 5.2.

4.3 Results

4.3.1 The time series

Time series were constructed from the data by binning and sampling at regular intervals. Any time bins when the source observation covered less than half a bin were not used; the remainder were corrected by the 'on-time' in each bin. As an illustration of the variability, Fig. 3 shows the full band, 0.3–10 keV, time series sampled at 256 s (for the PSD determination in each band, sampling times of 64 s were used). The frequent and periodic gaps in the data are clearly visible. The variability is clear, however, and even by eye it can be seen that it appears to have different characteristics in 2005 from the two observations in 2008. We quantify this in the next section.

4.3.2 Non-stationarity of the variations

The first *Suzaku* observation was obtained 3 years before the second two observations, when the source was in a substantially lower flux state. Even the second and third observations, taken 2 weeks apart, have different mean fluxes (Section 2). We therefore start by comparing power spectra from the three observations to test whether they are consistent with stationary behaviour or whether there are differences. Fig. 4 shows PSDs measured from each xis data set using the energy range of 0.3–10 keV, although because of the steep source spectrum and the higher effective area in the soft band, the measured spectrum is dominated by the soft band. The time sampling used was 64 s, with a bandpower interval of $\Delta \log_{10} \nu = 0.4$.
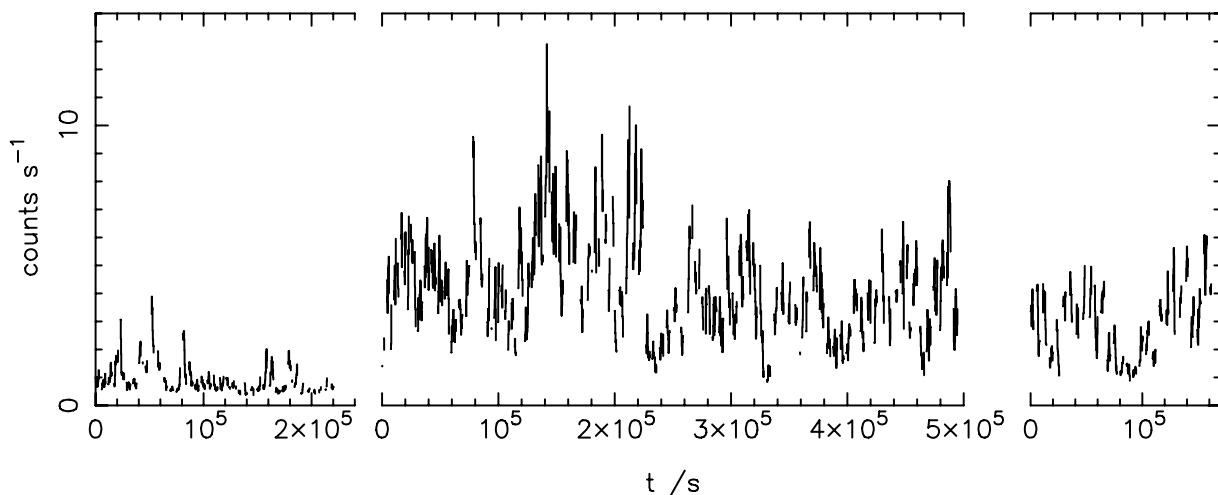
Figure 3. xis light curves, 0.3–10 keV, for the three *Suzaku* observations, sampled at 256 s: (left) 2005, (centre) 2008 November 6–12 and (right) 2008 November 23–25. The xis 0, 2, 3 observations of 2005 have been scaled to the flux expected in two detectors, to allow comparison with the xis 0, 3 measurements in 2008. Gaps indicate periods of no useful data. Time values are set to zero at the first period of useful data in each observation.
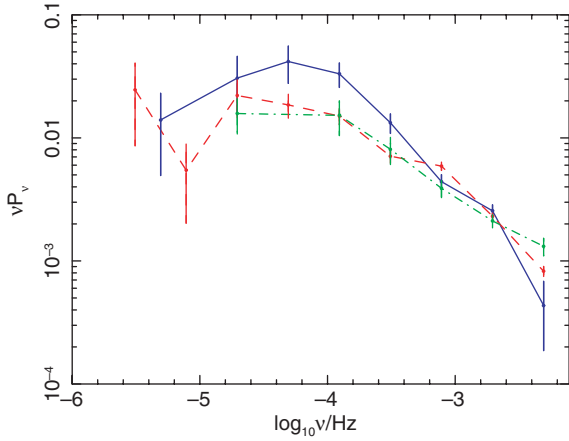
Figure 4. Comparison of the PSDs for NGC 4051 derived from the three epochs: 2005 (solid curve), 2008 November 6–12 (dashed) and 2008 November 23–25 (dot–dashed), showing $\log_{10} \nu P_\nu$ against $\log_{10} \nu$/Hz. Points with errors bars are plotted at the mid-point in $\log \nu$ of each band-power, error bars show the Fisher matrix uncertainties and lines are drawn to connect the points in each epoch of observation.

Bandpower intervals smaller than the window function full width (as defined in Section 4.1) were coadded as described above. The minimum frequencies differ for each data set owing to the differing lengths of observation (Table 1).

The PSDs at low frequencies, $\nu \lesssim 10^{-5}$ Hz, show significant variation owing to uncorrected red noise leak. Above this frequency however, useful comparison may be made. The two observations from 2008 are closely consistent with each other, the third observation having only a marginally significant excess of power at the highest frequency bandpower. The 2005 data appear significantly different however, with more power in the mid-frequency range and a steeper spectrum to high frequencies.

The mean levels used to normalize the fluctuations were different in the three data sets, of course. If we were to scale observations 2 and 3 to the same mean, their amplitudes would differ. This implies either what has previously been suggested (Uttley & McHardy 2001; Uttley, McHardy & Vaughan 2005) that the fluctuations are intrinsically 'fractional' in nature or that some intrinsic fluctuations

have been modulated by a secondary effect such as a varying multiplicative absorption. The 2005 observation, however, clearly has a different shape. To quantify this, we measure the slope of the PSD at high frequencies by fitting a linear relation between $\log P_\nu$ and $\log \nu$ for $\nu > 10^{-4}$ Hz. Such a functional fit is a good fit for the 2005 and 2008 November 23–25 PSDs but fits less well the 2008 November 6–12 PSD; as the aim of this exercise is to see whether there are statistically significant differences between the PSDs of the three epochs, this simple parametrization is sufficient. A minimum-χ^2-squared fitting method is adopted, where as well as taking account of the statistical uncertainty on each of the fitted PSD points, we also include the covariance between the points as determined from the Fisher information matrix. We find best-fitting slopes $\alpha = 2.00 \pm .08$, $1.78 \pm .03$ and $1.67 \pm .08$ for each of 2005, 2008 November 6–12 and 2008 November 23–25, respectively, where $P_\nu \propto \nu^{-\alpha}$. Thus, the two observations in 2008 have high-frequency slopes that are consistent with each other, but the 2005 PSD has a steeper high-frequency slope that differs by 2.7σ from the 2008 November 6–12 slope and by 3σ from the 2008 November 23–25 slope.

We return in Section 5 to discussion of these points in the full context of all the results, but for now we note that the PSD behaviour of the source appears non-stationary, given the different shape of PSDs between 2005 and 2008, and in the subsequent PSD analysis we treat the 2005 and 2008 data as separate time series.

4.3.3 Energy-dependent PSDs

To search for any dependence of PSD on photon energy, we divided the XIS photon events into six bandpasses covering the range of 0.3–10 keV. The likelihood method corrects for shot noise in the data, but as we shall be looking for differences between the PSDs of the six bandpasses, we have chosen energy boundaries such that each band has the same count rate. The source photon spectrum is steep, and the XIS effective area peaks in the soft band, so inevitably this means that the bands are not at all spaced evenly in energy. The energy bands were 0.3–0.94, 0.94–1.2, 1.2–1.5, 1.5–2.1, 2.1–3.8 and 3.8–10 keV.

The results are shown in Fig. 5 for a time sampling of 64 s. As found by McHardy et al. (2004), and as expected from the longer time-scale spectral variability in Section 3, the harder bands have
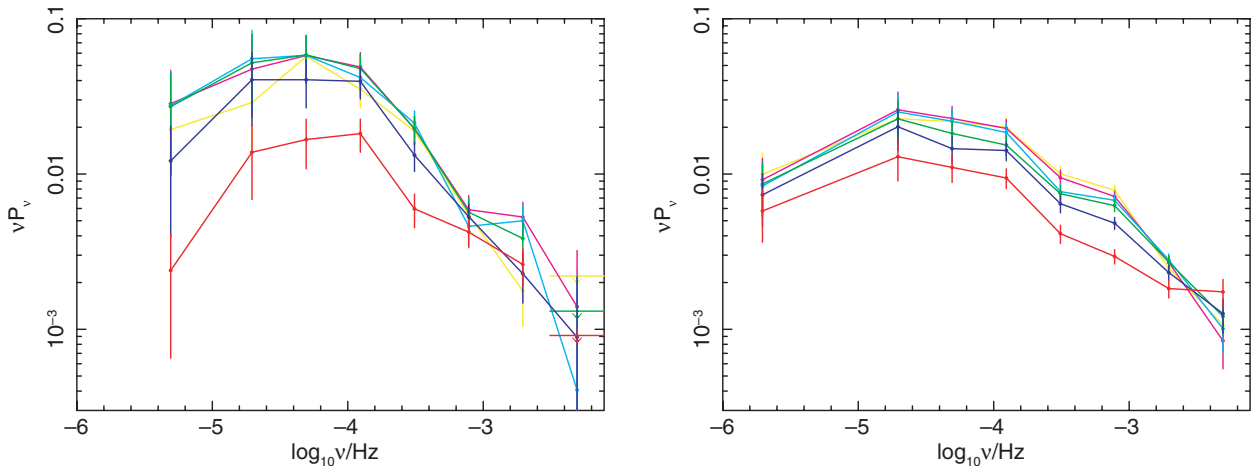

Figure 5. PSDs, plotted as $\nu P(\nu)$ from the observations of NGC 4051 in 2005 (left) and 2008 (right). There are six energy bands: 0.3–0.94 (yellow), 0.94–1.2 (magenta), 1.2–1.5 (cyan), 1.5–2.1 (green), 2.1–3.8 (blue) and 3.8–10 keV (red). The Fisher matrix uncertainties are shown as error bars. The PSD in the highest frequency bandpower in 2005 was consistent with zero in three of the energy bands; the plot shows the corresponding 2σ upper limits.

less overall variability. However, it is also clear that the hardest energy band, 3.8–10 keV, has a significantly flatter PSD than the softer bands, in fact having the highest power of any energy band at the highest frequency measured, despite having significantly lower power at lower frequencies, although given the error bars we cannot say that the hard band has significantly more power than the softer bands. This result is in good agreement with the model-fitting approach of McHardy et al. (2004) applied to the 2001 *XMM–Newton* data, where evidence for flattening of the PSD with energy was also found. Overall, the shape and normalization of the *Suzaku* PSD are in excellent agreement with those of the *XMM–Newton* PSD. There is some evidence that the lowest frequencies dip below the best-fitting relation $P(\nu) \propto \nu^{-1}$ found by McHardy et al. (2004), but the departure is consistent with the uncertainty in the McHardy et al. slope and in any case may be affected in our analysis by red noise leak. In the following analysis, we ignore the PSD shape at $\nu < 10^{-5}$ Hz.

4.3.4 Time delays and coherence

We can also search for evidence of time lags between energy bands, a phenomenon which has now been detected in a number of AGN, as discussed in Section 1. Again, we follow the method described by Miller (in preparation) where the cross-power spectrum between two bands is calculated in terms of some amplitude and a time lag between the bands. The value of time lag derived corresponds exactly to the time lag derived from the cross-correlation function in the case where every frequency bin is constrained to have the same lag. By working in the Fourier domain, however, we can also investigate frequency-dependent lags, effectively being the lags obtained by filtering the cross-correlation function with a top-hat filter in frequency. The lags we derive by this method are directly comparable to those derived by other authors (e.g. McHardy et al. 2004), but they have been arrived at by the maximum likelihood method rather than periodogram or Monte Carlo methods.

For this exercise, we combine all data sets to maximize the signal-to-noise ratio in the time lags. Even though the shape of the PSD varies between 2005 and 2008, the derived time lags show no significant evidence for epoch dependence; the 2008 data alone yield time lags very close to those from the combined data set, with slightly larger uncertainties. The 2005 data alone yield time lags consistent with the 2008 data but with large uncertainties. As found by McHardy et al. (2004), we find significant time lags between energy bands, where the harder band lags the softer band and where the lag increases with energy difference. We define the energy bands similarly to Section 4.3.3. Again, the bands have to be broad in energy in order to obtain an adequate count rate, but to best investigate the energy dependence of the time lags we relax the requirement to have equal count rates in all energy bands, and the hardest band from Section 4.3.3 is split into two: 3.8–6 and 6–10 keV. The time sampling chosen was 256 s: this longer time sampling improves the count statistics in each time bin, and we shall see from the results that we are most interested in time lags on periods longer than 1 ks and with values for the lag measured in hundreds of seconds. Accurate characterization of the measurement errors is important for the time delays, so here we supplement the standard Fisher matrix error measurements with direct measurement of the likelihood distribution, obtained by stepping through a range of time delays at each frequency, while maximizing the likelihood by allowing all other coefficients to vary. We define two confidence intervals by the regions $2\Delta \ln \mathcal{L} \leq 1$ and 2.7, respectively; as the likelihood distributions appear to be close to Gaussian, these correspond closely

Table 2. Time lags between the 0.3–0.94 keV band and bands at higher energy, as a function of time period T for the combined 2005–2008 data set.

T (ks)	Range (ks)	Lag (s)	Fisher error (s)	68 per cent error (s)	90 per cent error (s)
6–10 keV					
2879	51.2–162 000	−564	±913	+694 −715	+1163 −1190
28.8	16.2–51.2	970	±212	±225	+372 −374
9.1	5.12–16.2	299	±84	±86	±142
2.9	1.62–5.12	66	±35	±35	±58
0.91	0.512–1.62	30	±15	±17	±28
3.8–6 keV					
2879	51.2–162 000	−872	±711	+558 −563	+932 −942
28.8	16.2–51.2	700	±180	±193	±320
9.1	5.12–16.2	94	±59	±58	±95
2.9	1.62–5.12	57	±24	±24	±39
0.91	0.512–1.62	30	±9	±10	±16
2.1–3.8 keV					
2879	51.2–162 000	−880	±566	+474 −416	+767 −713
28.8	16.2–51.2	429	±124	±133	±219
9.1	5.12–16.2	57	±44	±44	±72
2.9	1.62–5.12	28	±16	±16	±26
0.91	0.512–1.62	12	±7	±7	±12
1.5–2.1 keV					
2879	51.2–162 000	−420	±477	+398 −351	+645 −600
28.8	16.2–51.2	373	±101	±106	±176
9.1	5.12–16.2	57	±35	±35	±57
2.9	1.62–5.12	7	±13	±13	±22
0.91	0.512–1.62	2	±6	±6	±11
1.2–1.5 keV					
2879	51.2–162 000	−444	±441	+343 −366	+582 −601
28.8	16.2–51.2	287	±101	±106	±176
9.1	5.12–16.2	48	±33	±32	±52
2.9	1.62–5.12	−1	±12	±12	±20
0.91	0.512–1.62	12	±5	±5	±9
0.94–1.2 keV					
2879	51.2–162 000	−427	±406	+317 −339	+537 −558
28.8	16.2–51.2	216	±108	±114	±189
9.1	5.12–16.2	49	±28	±27	±45
2.9	1.62–5.12	10	±11	±11	±19
0.91	0.512–1.62	6	±5	±5	±9

Note. Columns give the range of periods in each band and the lag, followed by three estimates of the errors: Fisher matrix, direct evaluation 68 per cent confidence region and direct evaluation 90 per cent confidence region. The longest time period in each energy band is likely affected by red noise leak and is not used in the analysis.

to the standard 68 and 90 per cent confidence regions of a normal distribution. The 68 per cent confidence regions are also close to the Fisher matrix errors, again as expected for Gaussian uncertainties. Table 2 gives the Fisher matrix and 68 and 90 per cent confidence regions for each frequency band.

In these results, lags of up to 970 s are detected with respect to the softest band that increase with band energy and with the period of the fluctuations, as found by McHardy et al. (2004). The longest period point is consistent with zero lag but with a very large uncertainty. Even so, it does appear discrepant compared with the results of McHardy et al. (2004) and is worth further consideration. McHardy et al. found a lag of 3000 s on time-scales of ∼70 ks between the
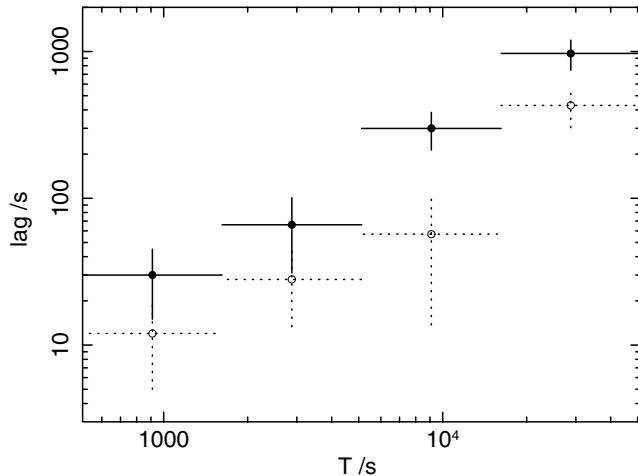
Figure 6. Time lags between the 0.3–0.94 keV band and the 6–10 keV (solid points and error bars) and 2.1–3.8 keV (open points and dotted error bars) bands, as a function of time period T for the combined 2005–2008 data set. Vertical error bars show the 68 per cent confidence regions. Horizontal bars show the range of time periods included in each bandpower.

0.1–0.5 and 5–10 keV bands. The disagreement with the 90 per cent confidence upper limit of 600 s (Table 2) could indicate a variation in source structure between 2001 and 2008; a more likely possibility, however, is that the long time-scales have not been sufficiently sampled by the *Suzaku* observations to allow accurate measurement, in contrast with the *RXTE* observations analysed by McHardy et al. (2004) that spanned 6 years. As discussed in Section 4.2, red noise leak into the longest period bin may corrupt the measurement of the time delay. We therefore exclude this bin from further consideration. Time lags between the 0.3–0.94 keV band and the 2.1–3.8 and 6–10 keV bands are shown in Fig. 6, plotted logarithmically (other bands are not shown, for clarity, but may be inspected in Table 2).

We also investigated time lags between the PIN and XIS bands; however, the PIN data were too noisy for any accurate time lag to be measured (although were consistent, within the large uncertainties, with the lags for the hardest band shown in Table 2).

Finally, we investigate the coherence, $\mathcal{R}$, between these two energy bands, where coherence is defined following Nowak & Vaughan (1996) as the ratio of the cross-spectrum amplitude squared to the product of the individual PSD amplitudes for the two bands, as a function of frequency. It is defined to lie in the range $0 \leq \mathcal{R} \leq 1$. High coherence implies that the different wavebands are highly correlated; low coherence implies that they are not. Fig. 7 shows $\mathcal{R}$ again as a function of frequency, showing only the Fisher matrix errors. The errors are large, so we have not directly measured the likelihood distributions in this case (because we only plot the Fisher errors, the error bars are not constrained to lie within the range $0 \leq \mathcal{R} \leq 1$). Results from the highest time period in 2005 are not shown as the uncertainty in $\mathcal{R}$ is of order unity. In the combined data set, 2005–2008, and in the 2008 data alone, the coherence is high at all frequencies. However, investigating the 2005 low state data alone, the coherence drops for short-period variations.

4.4 Summary of key timing analysis results

We now also summarize the key timing analysis results.

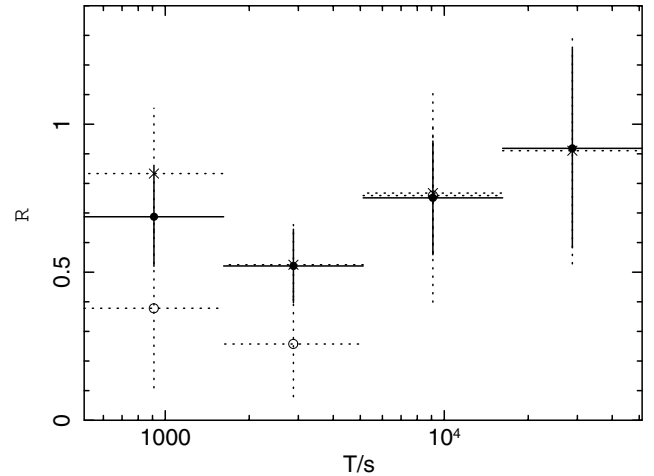(i) The PSDs demonstrate non-stationary behaviour between 2005 and 2008.

Figure 7. Coherence $\mathcal{R}$ between the 0.3–0.94 keV and 6–10 keV bands as a function of time period T for the combined 2005–2008 data set (solid symbols). Vertical error bars show the Fisher matrix errors and horizontal bars show the range of time periods included. Also shown are the coherence between the same bands for the 2005 data alone (open symbols and dashed error bars) and for the 2008 data alone (cross symbols and dashed error bars). The highest time period in the 2005 data set is not shown as the error bounds are too large to be useful.

(ii) The PSD measured for the hard band is significantly lower in amplitude and with a flatter frequency dependence than the soft-band PSDs, as previously found by other authors. The difference between bands is more marked in 2005 than in 2008.

(iii) We confirm the existence of both frequency-dependent lags of harder energy bands with respect to softer energy bands, up to 970 ± 225 s, and the energy dependence of the lags.

(iv) The coherence between soft and hard bands is high in the 2008 data, but is low in the 2005 data for short-period variations.

5 DISCUSSION

5.1 Comparison of timing results with previous observations

The power spectrum and frequency-dependent time lags measured from the *Suzaku* observations of NGC 4051 are in remarkably close agreement with the measurements reported by McHardy et al. (2004), despite being based on data taken with different observatories (*Suzaku* versus *XMM–Newton* and *RXTE*) on widely separated dates (2005–2008 versus 1996–2002) and using different analysis methods (maximum likelihood versus Monte Carlo). The key results that are in common are as follows.

(i) NGC 4051 is overall less variable at high energy than at low energy over most of the frequency range.

(ii) The high-energy PSD is flatter so that by time periods of about 128 s, the variability in each band is similar.

(iii) The softer bands in particular show a sharp break in the power spectrum at $\sim 10^{-4}$ Hz.

(iv) Frequency-dependent time lags are found, with the hard band lagging the soft band, with lag increasing with energy difference and with lag increasing with period. The maximum lag found in the *Suzaku* analysis is 970 ± 225 s for periods of tens of ks, similar to the maximum lag found by McHardy et al. (2004) on similar periods of approximately 800 s.

There are some differences: McHardy et al. (2004) found that the lag continues to increase with period, which may be attributable

to the much longer time baseline afforded by the 6 years of *RXTE* data they included, and they found a more significant decrease in coherence with a decreasing period which may be due partly to the difference in analysis methods and partly to the inclusion of low-state data in the McHardy et al. analysis. By analysing the 2005 low state separately from the 2008 higher state, we find significant differences in the PSDs and significantly lower coherence between bands in 2005.

5.2 Reverberation time delays

The frequency-dependent time delays in this and other AGN have previously been interpreted in terms of a model of intrinsic variations hypothesized to explain those features, comprising perturbations propagating inwards on an accretion disc where harder X-ray emission is emitted from smaller radii (Arévalo & Uttley 2006). While such models are not ruled out by the analysis presented here (the results largely agree with previous analyses), they do not have any predicted relationship to the PCA spectral decomposition that we have seen in Section 3, and although the earliest results indicated lags that varied linearly with the time period, more recent results reveal a more complex dependence of lag on period that has been interpreted as indicating the presence of multiple zones of fluctuating propagations (McHardy et al. 2007). However, there is a natural explanation of the frequency-dependent time delays in terms of reverberation delays (e.g. Peterson 1993) which we can relate directly to the PCA spectral components. In Section 3 we saw the existence of a hard component spectrum that dominates the low state, in common with many other AGN. If this component has a significant contribution from reflection, this may cause the observed time delays. In fact, reverberation models predict just the sort of frequency-dependent time delays that are observed here. We illustrate this with a simple model.

Let us suppose that at any frequency, the continuum flux we observe comprises two components: one a component from a central source that is seen directly and the other a time-delayed component reflected from distant material. Consider one Fourier mode of the measured source variability with angular frequency ω:

$$a'_\omega e^{i\omega(t-\tau')} = a_\omega e^{i\omega t} + a_\omega f \int_0^{\tau_{max}} b_\tau e^{i\omega(t-\tau)} d\tau, \tag{4}$$

where a_ω is the amplitude of that mode, τ is the time delay of reflected emission from some region, primed quantities denote the observed amplitude and time delay in the combined direct plus reflected signal, b_τ is the transfer function defined over the range $0 \le b_\tau \le \tau_{max}$ and f is the total reflected fraction of light. We expect $0 \le f < 1$ unless the illuminating source is obscured. It can be seen that the phase of the combined signal, contained in the term $e^{-i\omega\tau'}$, is related to the Fourier transform of the transfer function (see related results discussed by Peterson 1993). A simple case is given by considering reflection from a thin spherical shell of radius r; the transfer function is then a uniform probability distribution over the range $0 \le \tau \le \tau_s$ where $\tau_s = 2r/c$, and the imaginary part of equation (4), which is responsible for the observed time lags, is oscillatory. Smooth time lag functions may be produced by thick shells of reflection. A thick spherical shell, with uniform reflected light per unit radius within a range $r_1 \le r \le r_2$, has an observed phase term given by

$$\frac{a'_\omega}{a_\omega} e^{-i\omega\tau'} = 1 - i\frac{f}{\omega(\tau_{max} - \tau_1))} \int_{\tau_1}^{\tau_{max}} \frac{d\tau_s}{\tau_s}(1 - e^{-i\omega\tau_s}), \tag{5}$$

where we integrate over the thickness of the shell, defined by $\tau_1 = 2r_1/c$ and $\tau_{max} = 2r_2/c$. Fig. 8 illustrates the predicted delays, τ', as
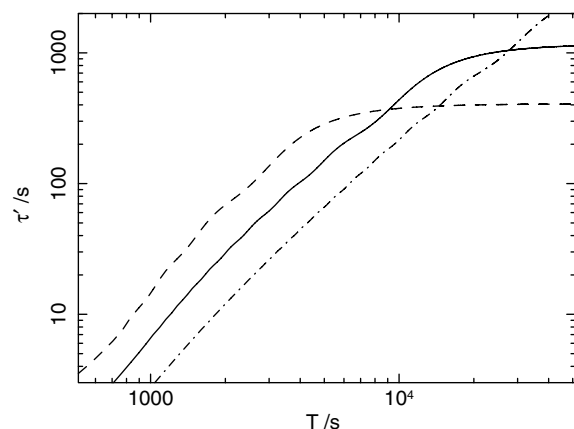

Figure 8. Predicted time lags, τ', from the simple thick-shell reverberation model as a function of the fluctuation time period T for $\tau_{max} = 10^{3.5}$ s (dashed curve), 10^4 s (solid curve) and $10^{4.5}$ s (dot–dashed curve). The reflection factor $f = 0.8$ for all curves.

a function of the fluctuation time period $T = 2\pi/\omega$ for $f = 0.8$, $\tau_1 = 500$ s and a range of values of τ_{max}. The frequency dependence arises because high-frequency modes are averaged out by the transfer function, and the remaining variability is thus more dominated by the illuminating source alone. Echoes of lower frequency modes can survive in the reflected signal, resulting in a measurable delay. The suppression of high-frequency modes in the reflected spectrum has an effect on the PSD, with the power in modes at $\omega \gtrsim 1/\tau_{max}$ being suppressed by a factor $(1 + f)^{-2}$ with respect to those at lower frequencies. The coherence between the direct signal and the combined direct plus reflected signal tends to unity at low and high frequencies and varies as $\cos^2(\omega\tau')$ at intermediate frequencies.

One particular point to note is that the measured time lags are significantly less than the light traveltime to the reflecting region, because the coaddition of primary and reflected light dilutes the time lag signature. In the limit $\omega \to 0$, the observed time lag tends to a maximum:

$$\tau' \to \frac{f}{4(1+f)} \frac{(\tau_{max}^2 - \tau_1^2)}{(\tau_{max} - \tau_1)}, \tag{6}$$

as seen in Fig. 8 at high time periods for the models with low τ_{max}, so $\tau' < \tau_{max}$ always, and in estimating the distance of the reverberating zone from the illuminating source we must allow for this dilution of the lag time.

It would be interesting if a signature of a maximum time lag could be found in the data. In NGC 4051 there is no evidence that such a maximum has been found, either in this analysis or in that of McHardy et al. (2004). However, a maximum lag has been found in Ark 564 (Arévalo et al. 2006; McHardy et al. 2007), lending support to the reverberation explanation. Another feature of the Ark 564 analysis is that at the highest frequencies there is some evidence for negative time lags (i.e. hard band leading soft band; McHardy et al. 2007) – in the reverberation model this may arise at high frequencies as a result of the time-lag oscillatory behaviour produced by a reflecting region that only partially covers the source. In effect, such apparent negative lags are an artefact created by the Fourier decomposition of the time lag signature.

To measure τ' in data, we need to be able to compare the combined, direct plus reflected, signal with the direct signal alone. In our measurements, we find a lag between hard-band photons and soft-band photons. If we assume that in the soft band we are seeing little reflected light, but that the hard-band signal is a combination
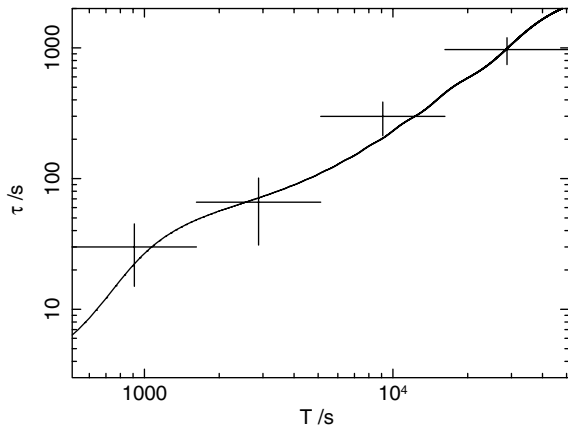
Figure 9. Predicted time lags, τ', from the two-component thick-shell reverberation model, with parameter values as described in the text, as a function of the fluctuation time period. Also shown are the measured hard-band lag values from Fig. 6. Note that this model is illustrative only and has not been fitted to the measured values.

of direct and reflected light, we may compare Fig. 6 with Fig. 8. It can be seen that there is good qualitative agreement between the simple reverberation model and the observed time lags, although the time lag for the shortest periods is larger than expected. The profile of the frequency dependence (the 'lag spectrum') depends on the assumed transfer function; a fall-off in reflection with radius as $1/r$, in either spherical or flattened geometries, tends to produce a flatter relation between lag and period. As a simple example of a more complex transfer function, we consider a two-component reflection model, in which an inner reflecting zone has parameters $f = 0.3$, $\tau_1 = 200$ s, $\tau_{max} = 800$ s and a second zone extending to larger radii has parameters $f = 0.8$, $\tau_1 = 800$ s, $\tau_{max} = 30\,000$ s, where these parameter values have been chosen purely as an illustration and have not been obtained from fitting to the data (there are three parameters that primarily affect the shape of the lag spectrum, and only four data points, so we do not consider fitting of this model to be particularly useful for this data set). In this particular illustration, the total reflected light exceeds the light that is directly received by the observer, implying some loss of direct light by either absorption or scattering. The resulting predicted lag spectrum is shown in Fig. 9 together with the measured hard-band time lags from Fig. 6. Such additional complexity in the reverberation model is able to reproduce more complex lag spectra, leading to the hope that improved data sets may be able to better constrain the distribution of circumnuclear material. Although accurate measurement of the lag spectrum could allow the transfer function to be determined, the present quality of data is insufficient to allow meaningful determination of the transfer function shape, and despite the lag excess on short time-scales, overall the simple thick-shell model provides a reasonable description of the present data set, and we now investigate the consequences of that simplest model.

To place statistical limits on the parameters of the simple thick-shell reverberation model, we used the frequency-dependent lag model of equation (5) within the likelihood maximization procedure to find best-fitting values of f and τ_{max}, stepping through a grid of f, τ_{max} values and evaluating the best-fitting likelihood for each grid parameter set. The value of the inner radius of reverberation is not well constrained by the data, and this was fixed at a value $\tau_1 = 500$ s. Confidence levels were assigned by finding intervals in log(likelihood), $\Delta\chi^2 = 2\Delta\ln\mathcal{L}$, of 2.3 and 4.61 corresponding to 68 and 90 per cent confidence intervals, respectively. The best-
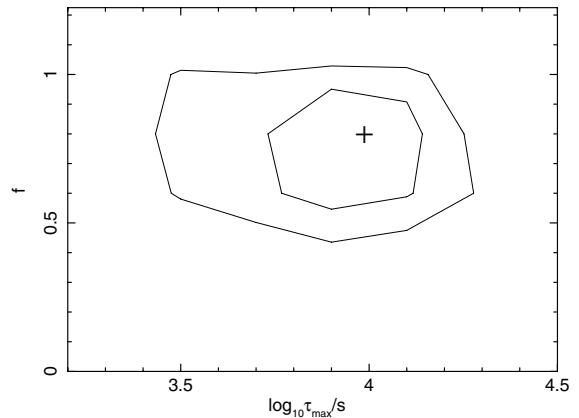

Figure 10. 68 and 90 per cent confidence intervals on the model parameters $\log_{10}\tau_{max}$ and f for the simple single-shell reverberation model as described in the text, derived from fitting to the combined 2005–2008 data set. The cross marks the best-fitting location.

fitting values for the lags between the 6–10 and 0.3–0.94 keV bands were $f = 0.8^{+0.15}_{-0.25}$, $\log_{10}\tau_{max} = 4.0^{+0.15}_{-0.3}$ (i.e. $\tau_{max} = 10\,000^{+4100}_{-5000}$ s), where quoted errors are 68 per cent confidence intervals, with a 90 per cent confidence range of $2500 < \tau_{max} < 20\,000$ s in τ_{max}. The confidence intervals are shown in Fig. 10. As $\tau_{max} = 2r_2/c$, the reverberating region extends to a distance $r_2 = 5000^{+2050}_{-2500}$ light-seconds in this model. We can see from consideration of Fig. 9 that the double-shell model produces more reflection from smaller radii (in the example shown, up to $r \lesssim 800$ s) but with additional larger scale reflection extending beyond the region where the current data can constrain its extent ($r \gtrsim 10\,000$ s). Irrespective of the detailed model, the continuous nature of the lag spectrum, lags monotonically increasing with time period, implies that there is thick-shell reverberation over a wide range of radii.

Overall, our conclusion is that reverberation naturally reproduces the frequency-dependent lags. The reflection fraction f may be directly interpreted in terms of the global covering factor of the source, C_g; in the case where our line of sight to the source is unobscured, $f = 0.8$ implies that the remaining sight lines are 80 per cent covered by material if it is 100 per cent reflective, when integrated through the reflecting zone, with higher covering factors for lower integrated reflection albedo. However, the inferred global covering factor is smaller if our line of sight is partially obscured, as this means that we could have overestimated f. In particular, if the covering fraction of our line of sight is the same as the global covering factor, and if that material transmits no light but has an albedo A, we expect $f \simeq AC_g/(1 - C_g)$ from which we would deduce $C_g = f/(A + f)$. Thus for $f = 0.8$ we deduce $C_g \gtrsim 0.44$ for $A < 1$.

The reverberation time lags we deduce in either the single-shell or more complex models place a significant component of reflecting material well within the broad-line region. In the case of the single shell model, it extends to distances $r_2 \simeq 1.5 \times 10^{14}$ cm or $600r_g$ (where $r_g = GM_{BH}/c^2$) with a 90 per cent confidence range of 150–$1200r_g$ for the nominal black hole mass of $M_{BH} = 1.7 \times 10^6\,M_\odot$. More complex models may have a component of reflection extending to larger radii, but this must be counter-balanced by enhanced reflection also at smaller radii. The most likely reflection configuration is discussed further in Section 5.6.

5.3 The reflection spectrum

McHardy et al. (2004) found that the time lags increase with the difference in energy between the bands being cross-correlated: harder
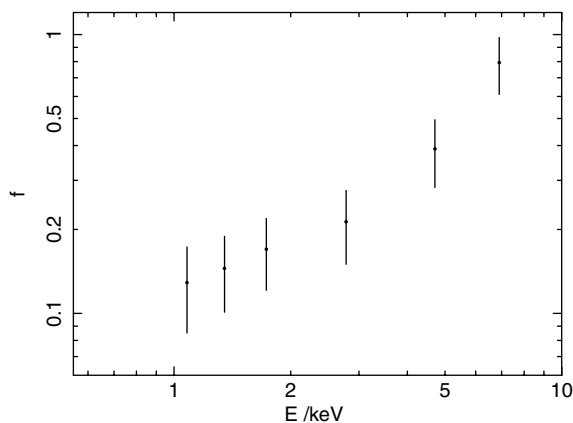
Figure 11. The variation in reverberation model reflection factor, f (the ratio of the reflected to directly received flux) with the median energy E of each band.

bands are more lagged with respect to softer bands. This is confirmed by the analysis here. In the reverberation model, this observation implies that the fraction f of reflected light increases with increasing energy. We can quantify this by fitting the simple 'single thick-shell' reverberation model to the time lags measured in various bands, and for a fixed model value of τ_{max} we can deduce f as a function of the energy band, again assuming that the softest band has a negligible reflection component. This is shown in Fig. 11 for the same energy bands used above, for the best-fitting value $\tau_{max} = 10^4$ s. The median photon energy in each band is plotted.

It is striking how similar the energy dependence looks to the spectrum of the offset component in the PCA analysis, which we have already interpreted as arising from a combination of absorption and reflection. We thus have a natural explanation, not only of the frequency dependence of the lags, but of their energy dependence also. The fall-off to low energy is a direct consequence of scattering in a medium whose opacity increases with decreasing energy. It is a generic feature of models of optically thick reflection (e.g. Magdziarz & Zdziarski 1995; Ross & Fabian 2005), but is expected to be seen also in the spectrum of scattered light in a less optically thick medium. A full calculation of Compton scattering in an extended, ionized, possibly clumpy, medium is required to make a full prediction of the expected spectrum. Of particular interest are the strength, line energy and profile of Fe Kα emission that would be expected. We saw in Section 3.2 that there exists a broadened component of Fe Kα on eigenvector one with an equivalent width of 66^{+43}_{-37} eV. If the reflected light accounts for a fraction $f/(1 + f)$ of the total observed light, for $f = 0.8^{+.15}_{-.25}$ we find that the equivalent width against the reflected component alone[2] would be about 150^{+113}_{-85} eV. This is significantly lower than would be expected for

---

[2] One caveat is that we need to be careful in interpreting the PCA components in this context: they were derived from spectral variability on time-scales longer than 20 ks, but in the reverberation signal we are studying variations on much shorter time-scales, and we do not know that the PCA spectral decomposition applies on these time-scales. If the long-period variations that shape the PCA are caused by partial-covering variation in the inner regions, some component of the reflection spectrum from the reverberating region could appear in the offset spectrum rather than being entirely contained within eigenvector one, and thus the true equivalent width of Fe Kα on the reflection component could be higher than estimated here. Unfortunately, we lack sufficient signal-to-noise to apply the PCA method to faster variations while retaining the spectral information.

reflection from neutral material, where equivalent widths of the order of 1 keV are expected (e.g. George & Fabian 1991), but in the environment close to the primary X-ray source we expect gas to be highly ionized, and such equivalent widths are produced in models of reflection in ionized material, for values of ionization parameter $\xi \gtrsim 100\,\mathrm{erg\,cm\,s^{-1}}$ (e.g. Ross & Fabian 2005). Two particular effects that would need to be taken into account in modelling the expected line emission are the effects of Compton scattering in a hot medium, which could significantly broaden the line, and the effects of resonant absorption and resonant line destruction in material where Fe is ionized to higher than Fe XVII (Matt, Fabian & Reynolds 1997; see also the review by Turner & Miller 2009 and references therein).

In practice, the reflection spectrum and the dependence of time lag on frequency would be expected to have a more complex inter-relationship than discussed in this simple model. Material close to the ionizing source would be expected to have a higher ionization, and hence be more reflecting at lower energies, than material further away. Long-period fluctuations would thus have reflection spectra characterized by lower ionization than the reflection associated with short-period fluctuations. The structure and geometry of the reflecting region could also have a significant effect on the reflected spectrum; for example, a clumpy two-phase medium could simultaneously produce a 'grey' reflection spectrum from fully ionized material and a hard reflection spectrum from lower ionization clumps, or a highly ionized reflecting region might itself be surrounded by lower ionization absorbing material. Such models could produce a wide range of spectrum hardness and emission-line equivalent widths. We postpone the investigation of more sophisticated models to future work.

5.4 Coherence and the amplitude of the PSD

The most noticeable feature of the comparison of the 2008 PSD between hard and soft bands is that the high energy bands show less fractional variability than the soft bands (i.e. the amplitude of the PSD is significantly higher in the soft bands compared with the hard band). The coherence in the overall data set is high, however, indicating that the same fluctuations are present in soft and hard bands but that their amplitude in the hard band is suppressed. Strangely, though, at the highest frequencies the soft and hard bands have comparable PSDs, with the hard-band variations possibly being even higher than the soft band, which does not fit easily with the simplest interpretations.

First, consider the expectation of the reverberation model. In the combined direct plus reflected signal the power spectrum is expected to be suppressed by a factor $(1 + f)^2$ at frequencies $\omega \gtrsim 1/\tau_{max}$, compared with the direct signal alone (Section 5.2). Thus if the soft-band PSD is dominated by intrinsic variations and the hard-band PSD is a reverberation-modified version of that, then we expect the 2008 hard-band PSD to be lower than the 2008 soft-band PSD by a factor of about $(1.8^{+.15}_{-.25})^2 \simeq 3.2^{+.6}_{-.8}$. This is consistent with the difference in PSD amplitudes at frequencies $10^{-5} < \nu < 10^{-3}$ Hz (Fig. 5) for $\tau_{max} \gtrsim 10\,000$ s.

However, this expected PSD amplitude difference was not observed at the highest frequencies, $\nu > 10^{-3}$ Hz, in 2008. Here, the hard band had at least as much variance as the softer band. It has previously been suggested that the flatter hard-band PSD is a result of the mechanism that produces the intrinsic fluctuations (e.g. Arévalo et al. 2006), which we have not addressed here. If we believe that the fluctuations we observe are intrinsic, the flatter PSD could be a consequence of that process. As an example of a possible effect that

could cause it, the highest frequency modes are likely not independent Gaussian fluctuations, but are more likely the high-frequency modes associated with sharp spikes of emission, so in this picture soft-band spikes might last longer than hard-band spikes. Without a more specific model for the emission process, it is difficult to make further progress on understanding the PSD. A future statistical analysis of non-Gaussianity in the time series may shed more light on the high-frequency behaviour.

The coherence of the hard- and soft-band signals may also aid our understanding. In 2008 the coherence was high at all frequencies, with a minimum coherence $\mathcal{R} \simeq 0.5$ at intermediate frequencies, rising to higher coherence at high, and probably at low, ω (Fig. 7). Reverberation is qualitatively expected to show similar behaviour (Section 5.2), but as the maximum observed value of $\omega\tau' \simeq 0.21$ (Table 2), the minimum coherence expected from reverberation alone is $\mathcal{R} = \cos^2(\omega\tau') \gtrsim 0.95$. Reverberation might make some contribution to the dip in $\mathcal{R}$ at intermediate frequencies, but overall the observed coherence values in the range $0.5 \lesssim \mathcal{R} \lesssim 0.9$ are more likely due either to imperfect intrinsic correlation between source fluctuations in the soft and hard bands or to some weak additional component of variability such as might arise from variable obscuration. Such effects cannot dominate, however, otherwise they would destroy the reverberation time lag signatures.

Turning to the 2005 low-state data, the PSDs have a different shape from the PSDs in 2008 (Section 4.3.3) and show both enhanced soft-band variability on longer time-scales and reduced coherence between the soft and hard bands. These two observations are indicative of an additional source of variability affecting the soft band but less so the hard band in 2005. Given the spectroscopic evidence that the central source was obscured in 2005 (Section 3), a strong candidate for that additional variability is varying absorption, either changes in column density and ionization or variations in covering fraction. A varying covering fraction of a clumpy absorber would match the longer time-scale spectral variability uncovered by the PCA. In the hard band, some variations arising from the absorber changes would be expected, but greatly reduced in amplitude because of the lower opacity at higher energies. As these variations would be uncorrelated with any intrinsic variations, the soft and hard bands would become more decorrelated, as observed (Fig. 7).

5.5 The absence of inner disc reflection signatures

In Section 3, we saw how there exists a hard component of emission which appears to be quasi-steady and essentially represents the low spectral state of the source. It is this component which, in mean spectra, leads to the existence of a 'red wing' at energies below the 6.4 keV Fe Kα line, and which has previously been widely interpreted as being highly redshifted reflection from the accretion disc close to or even inside the last stable orbit of the black hole. The general lack of variability of this component is problematic however, as its amplitude should vary with the amplitude of the illuminating continuum. To counter this expectation, Fabian & Vaughan (2003), Miniutti et al. (2003) and Miniutti & Fabian (2004) have proposed a model in which the continuum source is compact and lies close to the black hole. The source is hypothesized to move towards and away from the accretion disc; as it does so light rays follow geodesics in the space–time, and with careful placement it can be arranged that light reflected from the disc and reaching the distant observer can have an approximately invariant flux, while the flux from the source itself is low when the source is near the disc and high when it is further away.

The large time lags found here must however come from more distant material, and even though in NGC 4051 there *is* a component of hard excess that varies with the primary illumination, the reflecting material must be distant, not from the inner disc. We cannot rule out the existence of additional inner disc reflection, with essentially zero time lag, but given that we already need distant (lagged) reflection there is no justification for invoking an additional inner disc reflection component. Furthermore, the hard spectral component can be modelled quite satisfactorily as being caused by reflection and/or absorption from intervening material (e.g. in MCG−6-30-15; Miller et al. 2008, 2009; see also Terashima et al. 2009; Lobban et al., in preparation for discussion of NGC 4051). In the reverberation signal we find evidence for a high global covering factor of reflecting components, so all spectral features are accounted for.

5.6 Towards a complete picture of spectral variability

In this final discussion section, we attempt to collate the various observational results and interpret them in terms of the reverberation picture that has emerged in the previous sections. The aim is to build a complete model of the source spectral variability that is consistent between the spectral and timing analyses.

First, the difference between the 2005 and 2008 spectral states may be explained as being caused by obscuring material blocking a direct view of the central source so that the flux we see is dominated by reflection in 2005. This explains the strong invariant 6.4 keV Fe Kα line as well as the spectrum continuum shape if the line-emitting material continued to receive an invariant ionizing flux; that is, if most lines of sight other than ours remained open. Low, reflection-dominated states of NGC 4051 have previously been identified by Guainazzi et al. (1998), Pounds et al. (2004) and Terashima et al. (2009). The obscuration idea was proposed by Pounds et al. (2004) before the *Suzaku* data became available and is confirmed by the later observations. Guainazzi et al. (1998) and Terashima et al. (2009) also proposed an invariant reflection component, although their suggestion that its constant nature is due to light traveltime effects is not required if most of the transition between low and high flux states is caused by obscuring material along our line of sight to the central source. Because we did not have a direct view of the central source in 2005, any rapid variations would have been erased by reflection traveltime delays, causing the steeper cut-off to high frequencies in the 2005 PSD compared with the 2008 PSD (Figs 4 and 5). We do not have any good constraint on the location of the constant reflection component, however. The low coherence between soft and hard bands on time-scales of <5000 s and the large offset between the PSD amplitudes for the soft and hard bands in 2005 imply that the presence of a significant additional source of variability in the soft band, which we suggest is variable obscuration, most likely changes in the covering factor, during the 2005 observation.

Moving to the 2008 observations, the hard excess increased with the general brightening of the source. There are two possibilities. If the variable component of hard excess arises from reflection, but if the 2005 state was indeed due to obscuration, the postulated variable reflection component must also have been suppressed in 2005, i.e. it was also partially obscured along our sightline. This would be consistent with the partial-covering fitting by Terashima et al. (2009). There is evidence for a moderately broad component of Fe Kα that varied with the variable continuum (Sections 3.2 and 5.3). The variable hard excess and associated Fe Kα component would need to come from a region closer in than the region responsible for the steady, narrower Fe Kα so that it could be

obscured in this way. Alternatively, in 2008 we could still have been looking through some partially covering absorbing material that allowed transmission at high energy (as in PDS 456; Reeves et al. 2009) and which was suppressed in 2005 because of a higher column density. In either case, we require the hard excess to be partially obscured in 2005 and possibly in 2008 also. Both possibilities require obscuring and reflecting material to exist over a wide range of radii. Since 1998, the Fe Kα strength has been constant to within a factor of 2 (Terashima et al. 2009); as the emitting region may well be substantially smaller than 10 light-years, the implication is that the intrinsic illuminating continuum likewise has been constant to within this factor and that the larger amplitude continuum variability *on long time-scales* is due to variations in obscuration along our line of sight.

The time lags and their frequency and energy dependence indicate reverberation from reflecting material. The fraction of reflected light must be high, $f \simeq 0.8$ at $E \gtrsim 6$ keV, indicating a high global covering factor for this gas. Model fits of a thick reflecting shell imply that the reverberating zone is within a few light hours of the central source, extending over distances up to 5000^{+2050}_{-2500} light-seconds from the illuminating source. The spectrum of reflected light required to match the energy dependence of the lags is consistent with having the hard spectrum generically expected from reflected emission from ionized material. Obscuring and reflecting material may, and probably does, exist at larger distances, but we do not expect to see signatures of longer time lags in the timing analysis presented here, as longer time-scales would need to be probed. We note that reverberation signals are not created by variations in obscuration along the line of sight alone because most sight lines would be unaffected. Thus, the primary fluctuations whose echoes we see in the reflected light must either be intrinsic or, if due to varying obscuration, must be such that the majority of sight lines are affected.

The implications so far then are that long time-scale variations may be caused by changes in obscuration along the line of sight (likely to be partial-covering changes), but these variations on time-scales of days or less are most likely caused by an intrinsic mechanism. Because the coherence between energy bands is high in 2008 over the observed time-scales of days and less, and because we expect varying obscuration to be uncorrelated with intrinsic variations, there is not much room for both varying obscuration and intrinsic variability on these time-scales in the more common high states of the source, such as in 2008.

6 CONCLUSIONS

We have considered both the spectral variability and the broad-band variability power spectrum of three *Suzaku* X-ray observations of NGC 4051 spanning 3 years. We find and confirm many features from the spectral analysis and the power spectrum analysis that have been found by previous authors using independent data and methods, both in this AGN and in others. We have related the rapid variability features to the longer time-scale spectral properties and have shown that a self-consistent picture between these regimes is possible.

The interpretation of the long-term spectral variability of NGC 4051, previously noted by Guainazzi et al. (1998), Pounds et al. (2004) and Terashima et al. (2009), as being due to the primary X-ray source disappearing from view, leaving a constant, hard, reflection-dominated component, is confirmed here by the PCA, and we reiterate the suggestion that this is due to variable partial covering obscuring the central source during observed low states,

explaining the almost constant Fe Kα narrow-line flux. The PSD differs in the 2005 low state from that in the 2008 higher state, showing features consistent with this explanation.

We have detected the previously known time lags between hard and soft bands in the new *Suzaku* X-ray light curve of NGC 4051. Although previously hypothesized to be in some way related to the mechanism that produces X-ray emission, here we conclude that these time delays, and by inference those in other AGN also, are well described by reverberation from material up to a few light-hours from the central source. The important signatures are a strong dependence on the frequency of variations being measured and on photon energy, both of which have a natural explanation in the reverberation model. The frequency dependence is a consequence of observing superimposed direct and reflected components, and the measured lag–frequency relation is consistent with reverberation from a thick shell of material, although the precise geometry is not yet well constrained by the data. The measured energy dependence implies a hard reflection spectrum that is consistent with that expected from ionized material and which is also similar to the hard component that is seen in PCA of the spectral variations. To obtain sufficient reflection, the covering factor of reflecting material must be high, greater than about 0.44, as recently inferred from spectral modelling of other AGN (e.g. Miller et al. 2009). The existence of a maximum observed time lag at low frequencies and possible negative time lags at high frequencies, as observed in Ark 564 (Arévalo et al. 2006; McHardy et al. 2007), is expected in the reverberation model.

The identification of the signal as being reverberation confirms the idea that NGC 4051 and similar AGN are surrounded by substantial covering factors of optically thick, or nearly so, material within a few light-hours of the central source (far inside both the optical broad-line region and the dust sublimation radius). Although this AGN has a spectral hard-band excess very similar to that seen in other type I AGN, there is no requirement for any relativistically redshifted reflection from the inner accretion disc, which would not generate the observed time lags. The reverberating material extends over distances up to a few hundred gravitational radii from the illuminating source. Given the spectral and timing similarities with other type I AGN, we suggest that this source structure is a common feature of the type I population.

REFERENCES

Arévalo P., Uttley P., 2006, MNRAS, 367, 801
Arévalo P., Papadakis I. E., Uttley P., McHardy I. M., Brinkmann W., 2006, MNRAS, 372, 401
Arévalo P., McHardy I. M., Summons D. P., 2008, MNRAS, 388, 211
Bond J. R., Jaffe A. H., Knox L., 1998, Phys. Rev. D, 57, 2117
Denney K. D. et al., 2009, ApJ, 792, 1353
Efstathiou G., Moody S. J., 2001, MNRAS, 325, 1603
Fabian A. C., Vaughan S., 2003, MNRAS, 340, L28
Fukazawa Y. et al., 2009, PASJ, 61, 17
George I. M., Fabian A. C., 1991, MNRAS, 249, 352
Gruber D. E., Matteson J. L., Peterson L. E., Jung G. V., 1999, ApJ, 520, 124
Guainazzi M., Mihara T., Otani C., Matsuoka M., 1996, PASJ, 48, 781

Guainazzi M. et al., 1998, MNRAS, 301, L1

Iwasawa K. et al., 1996, MNRAS, 282, 1038

Koyama K. et al., 2007, PASJ, 59, 23

Kunieda H., Hayakawa S., Tawara Y., Koyama K., Tsuruta S., Leighly K., 1992, ApJ, 384, 482

Lamer G., McHardy I. M., Uttley P., Jahoda K., 2003, MNRAS, 338, 323

Lawrence A., Watson M. G., Pounds K. A., Elvis M., 1985, MNRAS, 217, 685

Lawrence A., Watson M. G., Pounds K. A., Elvis M., 1987, Nat, 325, 694

McHardy I. M., Green A. R., Done C., Puchnarewicz E. M., Mason K. O., Branduardi-Raymont G., Jones M. H., 1995, MNRAS, 273, 549

McHardy I. M., Papadakis I. E., Uttley P., Page M. J., Mason K. O., 2004, MNRAS, 348, 783

McHardy I. M., Arévalo P., Uttley P., Papadakis I. E., Summons D. P., Brinkmann W., Page M. J., 2007, MNRAS, 382, 985

Magdziarz P., Zdziarski A. A., 1995, MNRAS, 273, 837

Markowitz A., 2005, ApJ, 635, 180

Markowitz A., Papadakis I., Arévalo P., Turner T. J., Miller L., Reeves J. N., 2007, ApJ, 656, 116

Matsuoka M., Piro L., Yamauchi M., Murakami T., 1990, ApJ, 361, 440

Matt G., Fabian A. C., Reynolds C. S., 1997, MNRAS, 289, 175

Miller L., Turner T. J., Reeves J. N., George I. M., Kraemer S. B., Wingert B., 2007, A&A, 463, 131

Miller L., Turner T. J., Reeves J. N., 2008, A&A, 483, 437

Miller L., Turner T. J., Reeves J. N., 2009, MNRAS, 399, L69

Miniutti G., Fabian A. C., 2004, MNRAS, 349, 1435

Miniutti G., Fabian A. C., Goyder R., Lasenby A. N., 2003, MNRAS, 344, L22

Miniutti G. et al., 2007, PASJ, 59, 315

Mitsuda K. et al., 2007, PASJ, 59, 1

Nowak M. A., Vaughan B. A., 1996, MNRAS, 280, 227

Papadakis I. E., Lawrence A., 1993, MNRAS, 261, 612

Papadakis I. E., Nandra K., Kazanas D., 2001, ApJ, 554, L133

Peterson B. M., 1993, PASP, 105, 247

Pounds K. A., Reeves J. N., King A. R., Page K. L., 2004, MNRAS, 350, 10

Reeves J. N. et al., 2009, ApJ, 701, 493

Ross R. R., Fabian A. C., 2005, MNRAS, 358, 211

Russell D. G., 2004, ApJ, 607, 241

Takahashi T. et al., 2007, PASJ, 59, 35

Tanaka Y. et al., 1995, Nat, 375, 659

Terashima Y. et al., 2009, PASJ, 61, 299

Turner T. J., Miller L., 2009, A&AR, 17, 47

Turner T. J., Miller L., Reeves J. N., Kraemer S. B., 2007, A&A, 475, 121

Turner T. J., Miller L., Kraemer S. B., Reeves J. N., Pounds K. A., 2009a, ApJ, 698, 99

Turner T. J., Miller L., Reeves J. N., Lobban A., Kraemer S. B., Crenshaw D. M., 2009b, ApJ, submitted

Uttley P., McHardy I. M., 2001, MNRAS, 323, L26

Uttley P., McHardy I. M., Vaughan S., 2005, MNRAS, 359, 345

Vaughan S., Fabian A. C., 2004, MNRAS, 348, 1415

Vaughan S., Fabian A. C., Nandra K., 2003, MNRAS, 339, 1237

Wilms J., Reynolds C. S., Begelman M. C., Reeves J., Molendi S., Staubert R., Kendziorra E., 2001, MNRAS, 328, L27

This paper has been typeset from a TEX/LATEX file prepared by the author.